INTERNATIONAL JOURNAL FOR NUMERICAL METHODS IN FLUIDS
Int. J. Numer. Meth. Fluids 2001; **37**: 1–22 (DOI: 10.1002/fld.160)

Dissipative mechanism in Godunov-type schemes

Kun Xu[a,*,1] and Zuowu Li[b]

[a] *Mathematics Department, The Hong Kong University of Science and Technology, Clear Water Bay, Kowloon, Hong Kong*
[b] *Computational Fluid Dynamics Laboratory, Beijing University of Aeronautics and Astronautics, Beijing, China*

SUMMARY

This paper concerns the dissipative mechanism in the shock capturing schemes, where exact or approximate Riemann solvers are used in the flux evaluation. More specifically, we are going to analyze the dissipation in the flux vector splitting (FVS) scheme and the Godunov method, from which some pathological phenomena from the FVS scheme and the Godunov method will be explained, such as the artificial dissipation and the shock instability. Copyright © 2001 John Wiley & Sons, Ltd.

KEY WORDS: flux difference splitting; flux vector splitting; Riemann solver; shock instability

1. INTRODUCTION

In order to capture the discontinuous shock transition in the discretized space, the dissipation has to be introduced in the shock capturing schemes through physics or numerics. The shock capturing schemes include mainly the flux vector splitting (FVS) and the flux difference splitting (FDS) schemes. Even though both schemes have been successfully applied to a wide range of engineering problems, the dissipative mechanism in these methods has not yet been fully understood.

The flux vector splitting schemes are based on the splitting of flux function [11,14], where the flux at a cell interface has the form $F_{j+1/2} = F^{+}(W_j) + F^{-}(W_{j+1})$, where W_j and W_{j+1} are the left and right states at a cell interface. In the above flux construction, there is no any dynamical wave interaction between the left and right moving waves. In the present paper, we are going to qualitatively evaluate the dissipation underlying the above physical model. For example, the linear relationship between the numerical viscosity coefficient and the cell size, i.e. $v_{\text{num}} \sim \alpha \Delta x$, will be obtained. This linear relationship is intrinsically rooted in the above gas evolution model, which is even true for second-order MUSCL-type FVS schemes.

---

* Correspondence to: Mathematics Department, The Hong Kong University of Science and Technology, Clear Water Bay, Kowloon, Hong Kong. Fax: +852 23581643.
[1] E-mail: makxu@uxmail.ust.hk

Received November 1999
Revised November 2000

The exact Riemann solver implemented in the Godunov method accounts for the wave interaction in the gas evolution stage [3]. The dissipation is zero in the Riemann solution due to the use of the exact solution of inviscid equations. The numerical dissipation needed in the Godunov method to construct a shock thickness on the order of cell size is genuinely and mainly coming from the averaging process, i.e. the so-called initial reconstruction of constant state inside each cell [16]. For the multi-dimensional flow simulation, the numerical dissipation from the averaging depends on both the flow distribution and the mesh construction. In certain situations, the elimination of the physical and numerical dissipation in the Godunov method triggers the shock instability.

In this paper, Section 2 discusses a few numerical observations. Sections 3 and 4 present the explanation of the numerical observations and the analysis of the dissipative mechanism in both the FVS scheme and the Godunov method respectively. Section 5 concludes the paper.

2. NUMERICAL OBSERVATIONS

In this section, we are going to show a few numerical examples calculated by the Godunov and the van Leer FVS schemes. In order to clearly distinguish the dynamics from the reconstruction and gas evolution stages, an identical initial reconstruction method will be used for both schemes. In other words, any difference in the numerical solutions is solely due to the different dynamics in the flux functions.

2.1. Second-order Godunov and FVS schemes

Following van Leer's MUSCL idea [13], the numerical scheme is composed of an initial reconstruction stage followed by a dynamical evolution stage. At the beginning of each time step $t = 0$, cell averaged mass, momentum and energy densities are given. For a high-resolution scheme, interpolation techniques must be used to capture the subcell structure. In the current paper, the van Leer limiter is used to interpolate conservative variables directly.

Let $x_j = j\Delta x$ $(j = 0, 1, 2, \dots)$ be a uniform mesh and Δx the mesh size. Let $x_{j+1/2} = (j + 1/2)\Delta x$ be the interface between cells j and $j + 1$. The cell averaged conservative variable is denoted by $W_j = (\rho, \rho U, \rho V, \rho E)_j^T$, and its interpolated value in cell j is $\bar{W}_j(x)$, where the two pointwise values $\bar{W}_j(x_{j-1/2})$ and $\bar{W}_j(x_{j+1/2})$ are located at the locations $x_{j-1/2}$ and $x_{j+1/2}$. To second-order accuracy, the interpolated value in the jth cell can be written as

$$\bar{W}_j(x) = W_j + L(W_{j-l}, \dots, W_{j+l})(x - x_j) \quad \text{for} \quad x_{j-1/2} \le x \le x_{j+1/2}$$

where l is an integer and $2l + 1$ is the extent of the stencil. The van Leer limiter is used as the interpolating function L

$$L(s_+, s_-) = S(s_+, s_-)\frac{|s_+||s_-|}{|s_+| + |s_-|}$$

where $S(u, v) = \mathrm{sign}(u) + \mathrm{sign}(v)$ is defined in terms of sign-functions, and $s_+ = (W_{j+1} - W_j)/\Delta x$ and $s_- = (W_j - W_{j-1})/\Delta x$ are the corresponding slopes for the conservative variables.

In order to get a second order accuracy in time, we adapt the MUSCL-Hancock approach [12]. Based on the interpolated conservative variables $\bar{W}_j(x)$ inside cell j, the values of $\bar{W}$ at two end points inside cell j are denoted by $W_j^{\mathrm{L}} = \bar{W}_j(x_{j-1/2})$ and $W_j^{\mathrm{R}} = \bar{W}_j(x_{j+1/2})$. Firstly, the interpolated boundary values W_j^{L} and W_j^{R} are evolved by a half time step $1/2\Delta t$ according to

$$\bar{W}_j^{\mathrm{L}} = W_j^{\mathrm{L}} + \frac{1}{2}\frac{\Delta t}{\Delta x}\,[F(W_j^{\mathrm{L}}) - F(W_j^{\mathrm{R}})]$$

and

$$\bar{W}_j^{\mathrm{R}} = W_j^{\mathrm{R}} + \frac{1}{2}\frac{\Delta t}{\Delta x}\,[F(W_j^{\mathrm{L}}) - F(W_j^{\mathrm{R}})]$$

Then, based on the new states

$$W_{\mathrm{L}} = \bar{W}_j^{\mathrm{R}} \quad \text{and} \quad W_{\mathrm{R}} = \bar{W}_{j+1}^{\mathrm{L}}$$

the exact Riemann problem is solved in the Godunov method, from which the numerical fluxes can be obtained

$$F_{j+1/2}^{\mathrm{I}} = F(W_{j+1/2}(0)).$$

Here $W_{j+1/2}(0)$ denotes the value of $W_{j+1/2}(x/t)$ at $x/t = 0$, and I means the inviscid flux.

For the Navier–Stokes equations, we use a second-order central difference scheme to evaluate the viscous flux across a cell interface $F_{j+1/2}^{\mathrm{V}}$. The update of the conservative variables inside each cell becomes

$$W_j^{n+1} = W_j^n + \frac{\Delta t}{\Delta x}\,(F_{j-1/2}^{\mathrm{I}} + F_{j-1/2}^{\mathrm{V}} - F_{j+1/2}^{\mathrm{I}} - F_{j-1/2}^{\mathrm{V}})$$

For the van Leer FVS scheme, the only difference from the above Godunov method is that the flux function $F_{j+1/2}^{\mathrm{I}}$ is obtained according to the flux vector splitting formulation [14].

2.2. *Numerical results*

In this subsection, we are going to compare the numerical results from the second-order Godunov and van Leer FVS scheme in three test cases.

2.2.1. Shock structure calculation. The first test case is the standard Sod test case [10]. However, instead of solving the inviscid Euler equations, we solve the Navier–Stokes equations with unit Prandtl number directly, where the physical viscous coefficient ν_{phy} used in this case is set to be a constant $\nu_{\mathrm{phy}} = 0.0001$. With different cell sizes $\Delta x = 1/N$, where $N = 1600$, 3200, 6400, 10 000, the captured shock structures are shown in Figures 1 and 2 from both the second-order

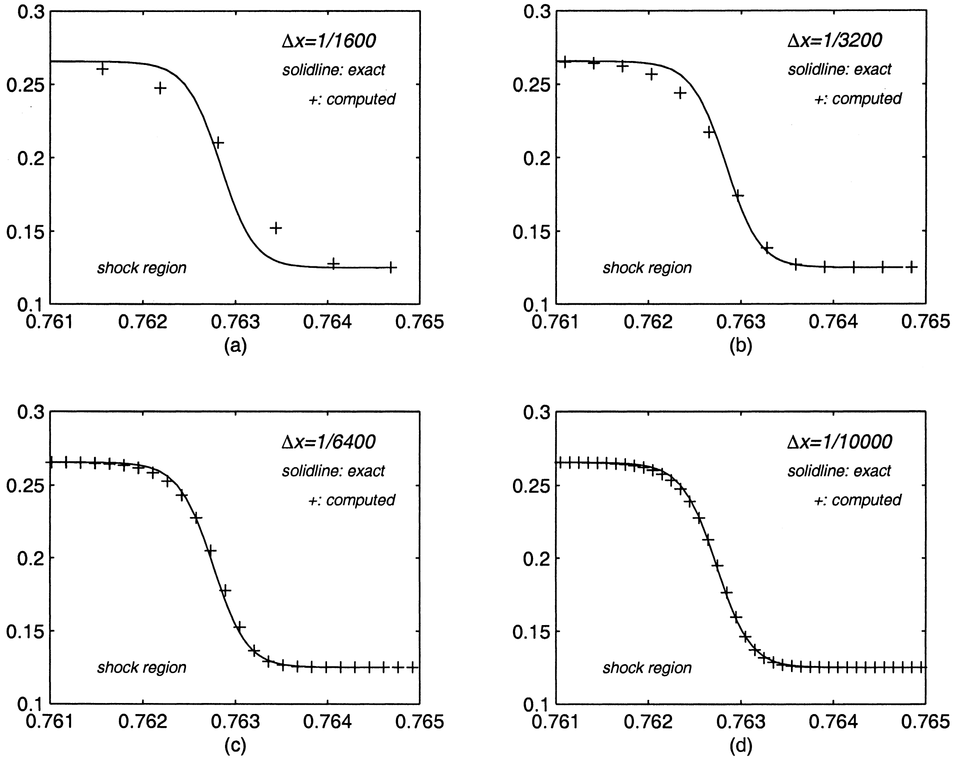

Figure 1. Density distributions in the shock region using the second-order NS Godunov method for the Navier–Stokes equations with $\nu_{\mathrm{phy}} = 0.0001$. The solid line is the exact NS solution. The cell sizes used are: (a) $\Delta x = 1/1600$; (b) $\Delta x = 1/3200$; (c) $\Delta x = 1/6400$; (d) $\Delta x = 1/10\,000$.

Godunov and the van Leer FVS schemes, where the solid line is the exact Navier–Stokes solution. The shock structures appear as mesh size goes down to 1/3200. The shock structures constructed from both schemes are equally matched. Since the kinetic flux vector splitting (KFVS) and FVS schemes have the same physical basis, it is not surprising that the Navier–Stokes KFVS scheme of Chou and Baganoff [1] can also give an accurate shock structure calculation.

2.2.2. Two-dimensional laminar boundary layer. In the following, we are going to test these schemes in a laminar boundary layer. The computational domain is covered by a uniform 320×120 grid points with the cell sizes $\Delta x = 1.0$ and $\Delta y = 1.0$. The flat plate is placed at the lower boundary ranging from $x_{\mathrm{start}} = 79.5$ to $x_{\mathrm{end}} = 320$ with total length $L = 240$. The inflow condition at $x = -\infty$ is

$$(\rho, U, V, p)|_{-\infty} = \left(1, 3, 0, \frac{9}{\gamma M^2}\right)$$

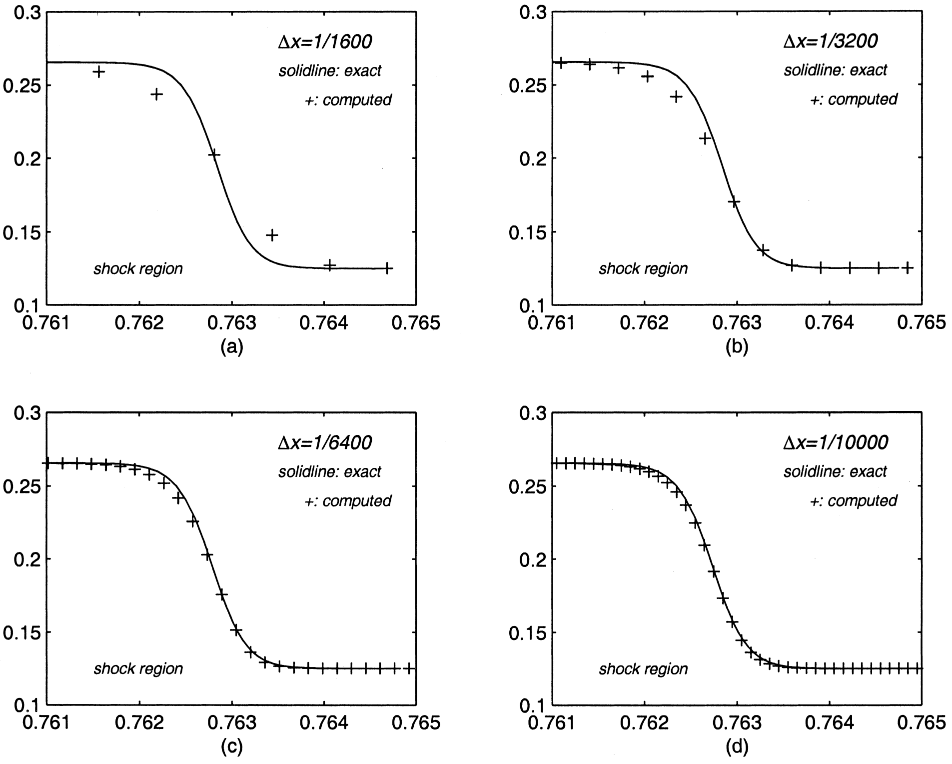

Figure 2. Density distributions in the shock region using the second-order NS van Leer FVS method for the Navier–Stokes equations. The solid line is the exact NS solution. The cell sizes used are: (a) $\Delta x = 1/1600$; (b) $\Delta x = 1/3200$; (c) $\Delta x = 1/6400$; (d) $\Delta x = 1/10\,000$.

where M is the fixed Mach number with the value $M = 0.3$ and $\gamma = 1.4$. In this test case, the Reynolds number is defined by $Re = UL/\nu_{\text{phy}}$, which is equal to $Re = 30\,000$ with the choice of $\nu_{\text{phy}} = 0.024$.

No-slip boundary condition is imposed on the flat plate by creating two 'ghost' cells outside the computational domain which reverse the velocities of the two cells above the flat plate. The Euler boundary condition with x-direction velocity slip is used for the other part of the lower boundary. An appropriate non-reflecting boundary condition based on the one-dimensional Riemann invariants is used at the left and upper boundaries. For example, in the left boundary, based on the Riemann invariants

$$R_1 = U_{-\infty} + \frac{2C_{-\infty}}{\gamma - 1} = U_0 + \frac{2C_0}{\gamma - 1}$$

and

$$R_2 = U_1 - \frac{2C_1}{\gamma - 1} = U_0 - \frac{2C_0}{\gamma - 1}$$

where subscript '1' refers to the first cell inside the computational domain, we can determine the velocity U_0 and the sound speed C_0 in the first cell outside the left boundary. Also, with the help of the entropy invariant condition

$$\frac{p_{-\infty}}{\rho^{\gamma}_{-\infty}} = \frac{p_0}{\rho^{\gamma}_0}$$

we can determine other conservative variables at the cell 0. The flow variables in the cell -1 are set to be equal to the corresponding values at the cell 0. Simple extrapolation of the conservative variables is used at the right boundary.

The output normalized u velocity

$$u = U/U_{\infty}$$

are taken at the locations $x = 150$, 200, and 250, and the distance y above the flat plate is normalized by

$$\eta = y\sqrt{\frac{U_{\infty}}{\nu_{\text{phy}}(x - x_{\text{start}})}}$$

Figures 3 and 4 show the u velocity distributions calculated by the Godunov and the van Leer FVS schemes. The solid line is the exact Blasius solution. As shown in these figures, the Godunov method can give accurate laminar boundary solution, while the FVS scheme can hardly capture the correct shear layer. Since we have used the same initial reconstruction

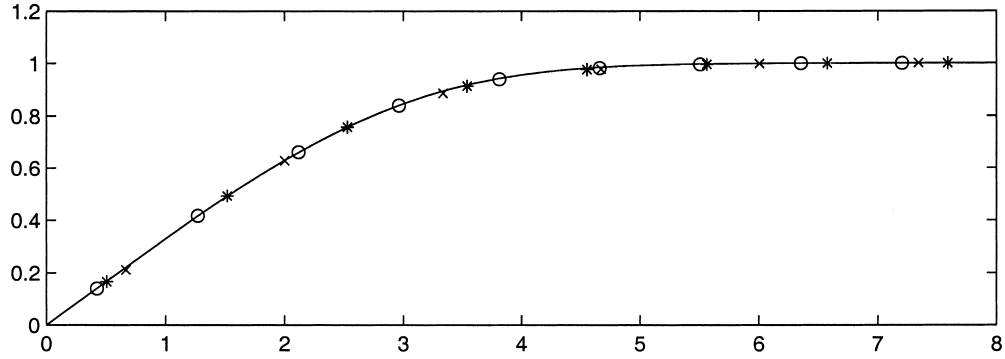

Figure 3. u velocity distribution versus η obtained using the second-order NS Godunov method. The output locations are at: ($\times$) $x = 150$; (*) $x = 200$; (○) $x = 250$. The solid line is the exact Blasius solution.

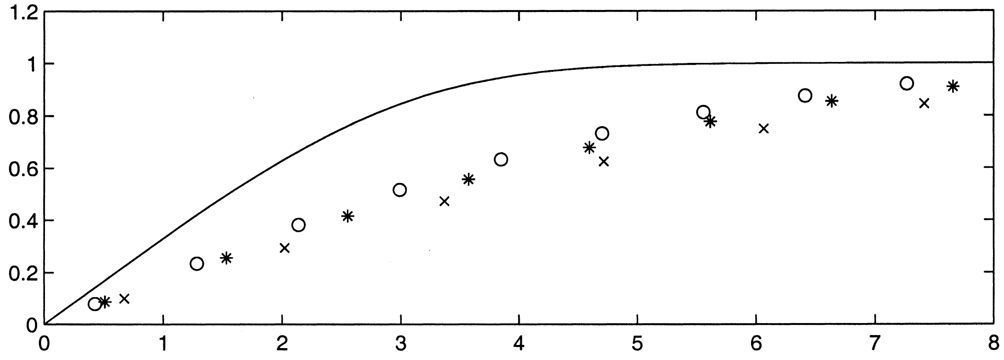

Figure 4. u velocity distribution versus η obtained using the second-order NS van Leer FVS method. The output locations are at: (×) $x = 150$; (*) $x = 200$; (○) $x = 250$. The solid line is the exact Blasius solution.

technique in both schemes, the different behavior between the Godunov and FVS methods must come from the gas evolution model, i.e. the dissipative mechanism underlying the flux evaluation. A detail analysis will be presented in the next section.

Recently, Chou and Baganoff proposed a Navier–Stokes KFVS scheme [1]. In their paper, they have tested the shock layer and showed that their NS KFVS scheme gives an accurate NS solution. However, applying the Chou–Baganoff scheme to the above boundary layer problem, we find that their scheme behaves basically in the same way as the van Leer FVS scheme. The u velocity distribution is shown in Figure 5.

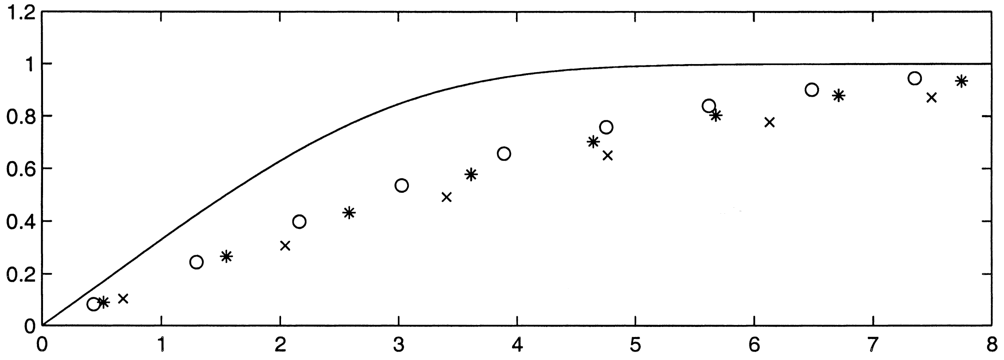

Figure 5. u velocity distribution versus η obtained using the second-order NS Chou–Baganoff KFVS method. The output locations are at: (×) $x = 150$; (*) $x = 200$; (○) $x = 250$. The solid line is the exact Blasius solution.

2.2.3. Odd–even decoupling case. Quirk [7] cataloged a few cases, which could trigger the failure of upwinding schemes. In the following we test both the second-order Godunov and FVS schemes in the odd–even decoupling case. This test is about a normal shock propagating in the two-dimensional shock tube, where the location of central line is perturbed odd–evenly with a magnitude of 10^{-6}. As shown in Reference [7], any small fluctuation gets amplified quickly in the Roe scheme [8], and the initial shock front is totally destroyed after the shock propagating through some distance in the tube. Figure 6(a) shows the result from the second-order Godunov method for solving the inviscid Euler equations, and Figure 6(b)–(d) are from the Godunov method solving the corresponding Navier–Stokes equations. Figure 6(e) presents the result from the FVS scheme for the inviscid Euler equations. From these figures, we can clearly observe that the Godunov method amplifies small perturbation and gives large post-shock oscillations, and the shock instability is effectively removed by solving the viscous governing equations. On the other hand, even solving the inviscid Euler equations, the FVS scheme gives a non-oscillatory density distribution.

2.3. Summary

The above numerical observations show: (1) the Godunov and the FVS schemes behave both nicely in the shock structure calculations; (2) the Godunov method does a good job in boundary layer calculation, but the FVS scheme behaves poorly; (3) the FVS scheme has intrinsic dissipation to suppress small flow perturbation in the strong shock case, and the Godunov method does not. In the next sections, we are going to explain these observations and analyze the dissipative mechanism in both schemes.

3. DISSIPATIVE MECHANISM IN THE FVS SCHEME

3.1. Numerical dissipation in the FVS flux function

Similar to the KFVS scheme, all FVS schemes have the same particles or waves free transport mechanism. Physically, it means that the FVS scheme has the particle mean free path $\bar{l}$ be equal to the cell size Δx. Since the viscosity coefficient $\bar{v}$ is proportional to the mean free path, i.e. $\bar{v} \sim \bar{c}\bar{l}$, where $\bar{c}$ is the local sound speed, the artificial viscosity coefficient $\bar{v}$ in the FVS scheme is therefore proportional to the cell size Δx, i.e. $v_{\text{num}} = \alpha \Delta y$ or $v_{\text{num}} = \alpha \Delta x$ [15].

In order to verify the above analysis, we have done a mesh refinement study in the boundary layer case for the FVS scheme. The computation is done using the FVS scheme for the inviscid Euler equations directly, and the no-slip boundary condition is imposed on the flat plate by reversing the fluid velocities in the ghost cells. The numerical viscosity coefficient v_{num} in the FVS scheme is obtained by fitting its solution with the Blasius solution.

In Table I, we list the experimental data of the cell size Δy and the corresponding viscosity coefficient. Figure 7 shows this fitting process to get the above numerical viscosity coefficients. As shown in Figure 7, at $\Delta y = 1/3$, the numerical boundary layer thickness from the FVS scheme is thinner than the reference solution with $v_{\text{phy}} = 0.024$, so the numerical viscosity v_{num} is smaller than v_{phy}. Figure 8 plots the data in Table I and clearly shows the linear dependence between the cell size Δy and the numerical viscosity coefficient v_{num}. Based on the numerical

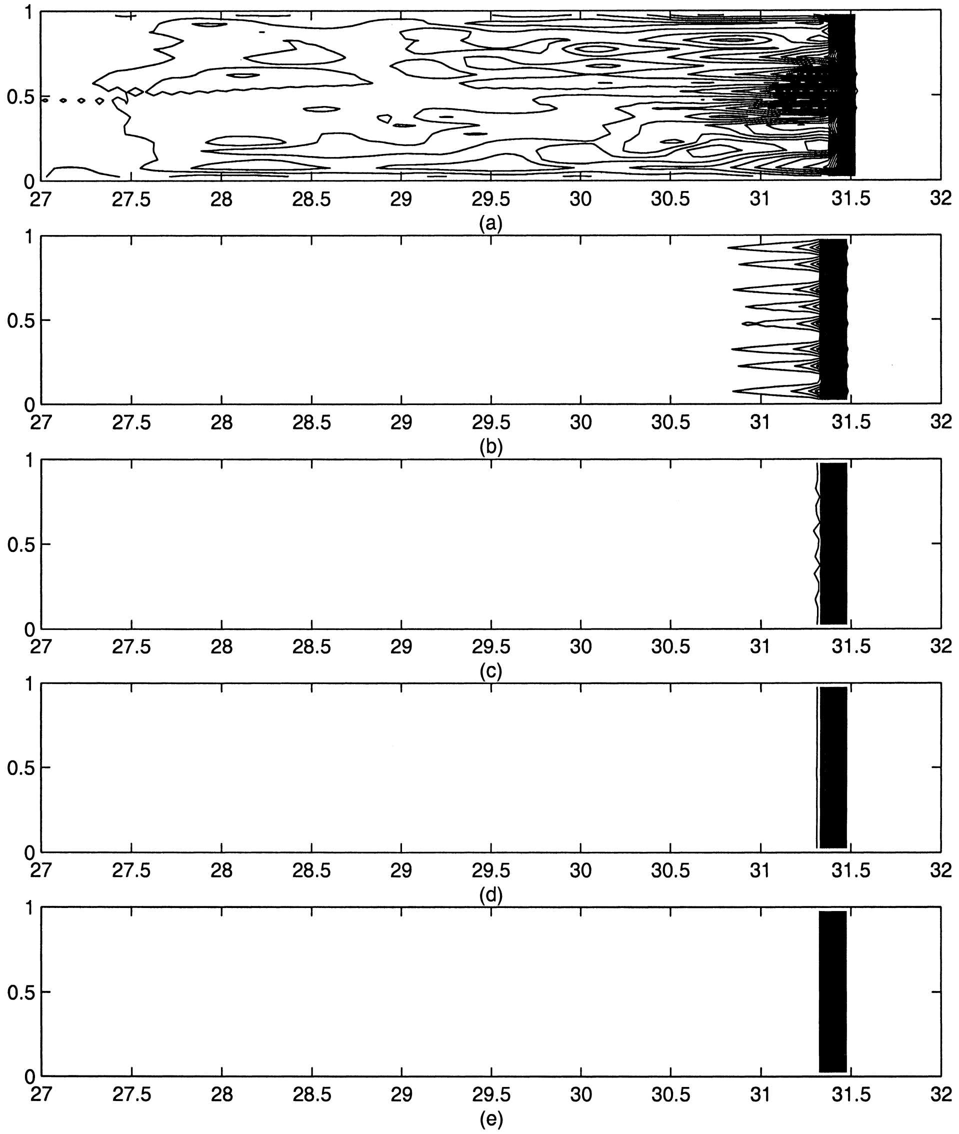

Figure 6. Density distributions of the two-dimensional Quirk problem [7], where the location of the central line is perturbed odd–evenly. (a)–(d) are obtained using the second-order NS Godunov method with: (a) $\nu_{\text{phy}} = 0.0$ (inviscid Euler solution); (b) $\nu_{\text{phy}} = 0.0005$; (c) $\nu_{\text{phy}} = 0.001$ and (d) $\nu_{\text{phy}} = 0.0012$. The density distribution in (e) is obtained using the second-order van Leer FVS scheme with $\nu_{\text{phy}} = 0.0$.

Table I. The viscosity coefficient versus cell size, where $\nu_{\text{phy}} = 0.024$ is a reference.

Δy	1	2/3	1/2	1/3
$\sqrt{\nu_{\text{num}}/\nu_{\text{phys}}}$	1.9	1.45	1.17	0.86

data, we get the proportional coefficient $\alpha \simeq 0.11$. This number is on the same order as the theoretical analysis in Appendix A. If the Godunov method for the inviscid Euler equations is used in the current study, even with the imposed no-slip boundary condition, it does not form any boundary layer at all. In other words, even in the first cell above the flat plate, the fluid velocity will keep the value of $U_{-\infty}$. Therefore, the exact Riemann solver has intrinsic $\nu_{\text{num}} = 0.0$ in this case.

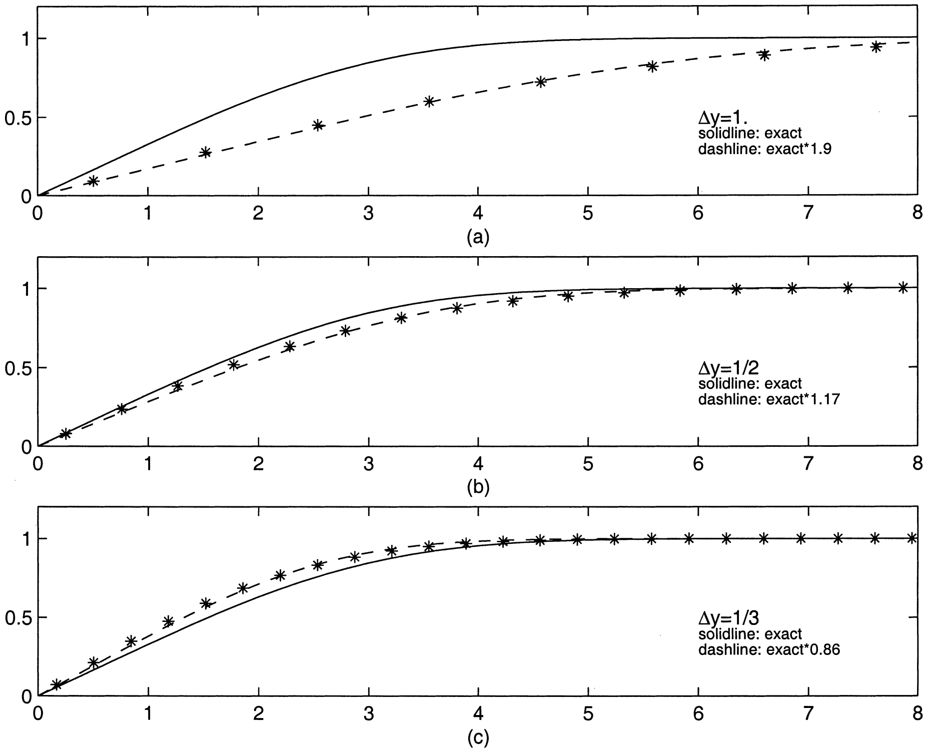

Figure 7. Mesh refinement study of the van Leer FVS scheme for the inviscid Euler solutions in the laminar boundary layer case, where no-slip boundary is imposed at the flat plate. The above boundary layer is constructed purely from the numerical viscous effect. The dashline is obtained by changing the viscosity coefficient of the Blasius solution to fit the numerical data at the location of $x = 200$. The solid line is the exact Blasius solution with $\nu_{\text{phy}} = 0.024$, which can be considered as a reference solution.

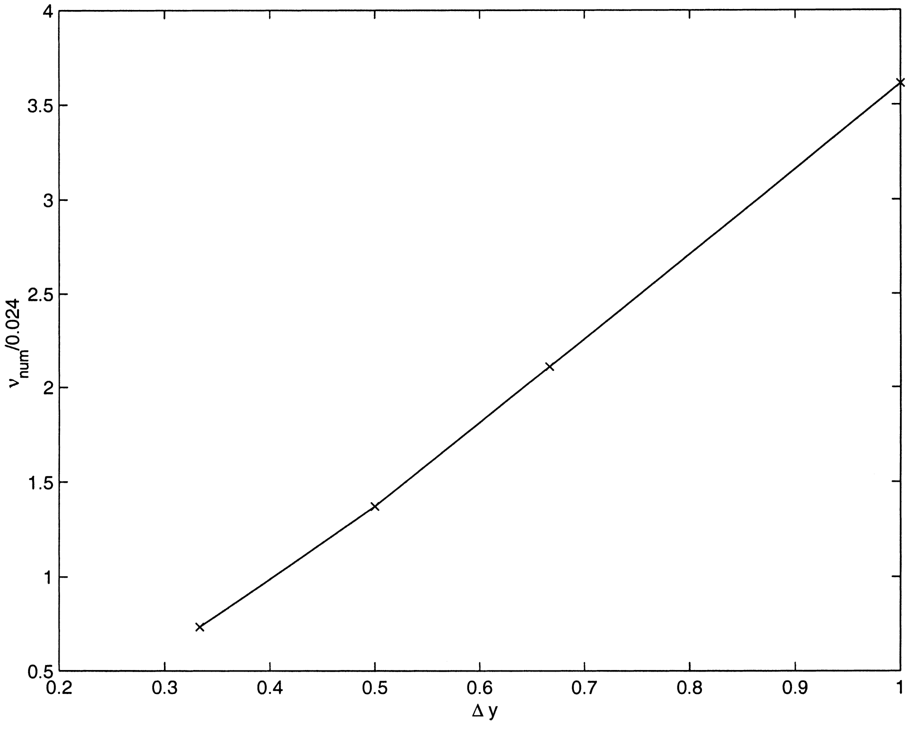

Figure 8. The numerical viscosity coefficient $\nu_{\text{num}}/0.024$ versus mesh size Δy for the solutions in Figure 7.

From this experiment, we can understand that the free transport mechanism underlying the FVS scheme generates first-order dissipation. This is the basic reason for the robustness of the FVS scheme, such as avoiding the shock instability. The FVS scheme is actually solving viscous governing equations in the gas evolution stage due to its flux splitting mechanism $F = F^+ + F^-$.

In order to capture the Navier–Stokes solutions, adaptive mesh is usually used in the boundary layer calculations, where the mesh size is very small in the boundary layer and large away from the boundary. If the FVS scheme is used here, due to the difference in the cell size, the dissipation coefficient ν_{num} will be different at different locations of the boundary layer. As a result, the similarity solution will be most likely lost, such as figure 10(a) shown in [2]. In our case, since we are using a uniform mesh, the numerical viscosity coefficient keeps a constant everywhere. Therefore, the similarity solution from the FVS scheme can be maintained, such as the results shown in Figure 7.

The relationship $\nu_{\text{num}} \sim \alpha \Delta x$ is an intrinsic property of the FVS scheme. Even inside a shock layer, this relation is still correct. Also, this relationship does not mean that the FVS scheme cannot be used for the Navier–Stokes solutions. The condition for its use is that the physical viscosity coefficient in the Navier–Stokes equations should be much larger than the numerical one, i.e. $\nu_{\text{phy}} \gg \alpha\Delta x$. As analyzed in the next subsection, this is true in the shock structure calculation.

3.2. Different behavior of the FVS scheme in shock and boundary layers

As observed in Section 2, the FVS scheme behaves differently in the shock and boundary layer calculations. The explanation can be the following.

Suppose we need $N \sim 10$ cells to resolve the physical shock structure and the boundary layer. Then, the shock thickness l_{s} can be expressed as

$$l_{\text{s}} \sim \frac{\nu^{\text{s}}_{\text{phy}}}{\Delta U} \sim N\Delta x$$

where s means the shock case, and ΔU is the velocity jump. For the boundary layer, the thickness l_{b} becomes

$$l_{\text{b}} \sim \sqrt{\frac{\nu^{\text{b}}_{\text{phy}} L}{\Delta U}} \sim N\Delta x$$

where b means boundary. In both cases, ν_{phy} refers to the physical viscosity coefficient. In the boundary layer case, ΔU is the velocity jump from the surface of the flat plate $U = 0$ to the velocity U_∞ at far upstream, and L is the length of the flat plate. Note that the velocity jump in both shock and boundary cases can be considered on the same order as the test cases presented in Section 2. From the above equations, the physical viscosity coefficients in both the shock and boundary layers become

$$\nu^{\text{s}}_{\text{phy}} \sim N\Delta x\Delta U \quad \text{and} \quad \nu^{\text{b}}_{\text{phy}} \sim \frac{(N\Delta x)^2 \Delta U}{L}$$

Suppose that we use the FVS scheme to simulate shock and boundary layers. Because the numerical dissipation coefficient in the FVS scheme is proportional to the cell size in both flow situations, i.e. $\nu_{\text{num}} \sim \alpha\Delta x$, the ratio between the numerical and physical viscosity coefficients are

$$\left.\frac{\nu_{\text{num}}}{\nu_{\text{phy}}}\right|_{\text{shock}} \sim \frac{\alpha}{N\Delta U} \tag{3.1}$$

in the shock region, and

$$\left.\frac{\nu_{\text{num}}}{\nu_{\text{phy}}}\right|_{\text{boundary}} \sim \frac{\alpha L}{N^2 \Delta x \Delta U}$$

in the boundary layer case. Since $L \sim N^2 \Delta x$ in our boundary layer calculation in Section 2, the above relation goes to

$$\left.\frac{\nu_{\text{num}}}{\nu_{\text{phy}}}\right|_{\text{boundary}} \sim \frac{\alpha}{\Delta U} \tag{3.2}$$

Comparing Equations (3.1) and (3.2), for the same amount of the numerical dissipation, the numerical viscosity plays a much more important role in the boundary layer than that in the shock layer once both layers are well resolved, such as $N \sim 10$ grid points in both layers.

The good behavior of the FVS scheme in the shock structure calculation can be also understood in the following. Because the physical shock thickness l_s is on the order of particle mean free path, in order to resolve it by N numerical cells the cell size Δx must be much less than l_s, such as $\Delta x \ll l_s = N\Delta x$. However, the numerical dissipation in the FVS scheme is coming from the free transport on the scale of numerical mean free path Δx. Since the numerical mean free path is much less than the physical mean free path, the relation $\alpha/(N\Delta U) \ll 1$ is always true in the shock structure calculation. But, $\alpha/\Delta U$ is not necessarily a small number in the boundary layer calculation.

4. DISSIPATIVE MECHANISM IN THE GODUNOV METHOD

4.1. Dissipative mechanism in the Godunov method

The Godunov method is based on the exact Euler solution, the so-called Riemann problem in the gas evolution stage. The Riemann problem is defined as an initial value problem for the Euler equations. In the one-dimensional case, with the following initial condition at $t = 0$

$$(\rho, U, p) = \begin{cases} (\rho_L, U_L, p_L) & x \leq 0 \\ (\rho_R, U_R, p_R) & x > 0 \end{cases} \tag{4.3}$$

A entropy-satisfying solutions of the Riemann solver consist of the wave structure: the left state (ρ_L, U_L, p_L) is connected to the right state (ρ_R, U_R, p_R) by a 1-shock or 1-rarefaction wave, a 2-contact discontinuity, and a 3-shock or a 3-rarefaction wave. The 2-contact discontinuity separates two constant states (ρ_I, U^*, p^*) and (ρ_{II}, U^*, p^*), and (U, p) are continuous across the contact discontinuity. For example, in Figure 9 the 1-wave is a rarefaction and the 3-wave a shock. There is standard technique to obtain the solutions around a contact discontinuity [12]. The physical dissipation in the Riemann solver is coming from the formation and propagation of the shock waves. As shown in Figure 9, when fluid particles across the shock wave, the entropy increase is automatically achieved. However, the above physical dissipation only plays a minimal role in the construction of the numerical shock thickness, which is on the order of cell size. For example, for a single stationary shock, if the shock front is located exactly on the cell interface, the Godunov method could keep this solution forever. In other words, the physical dissipation provided in the shock wave of the

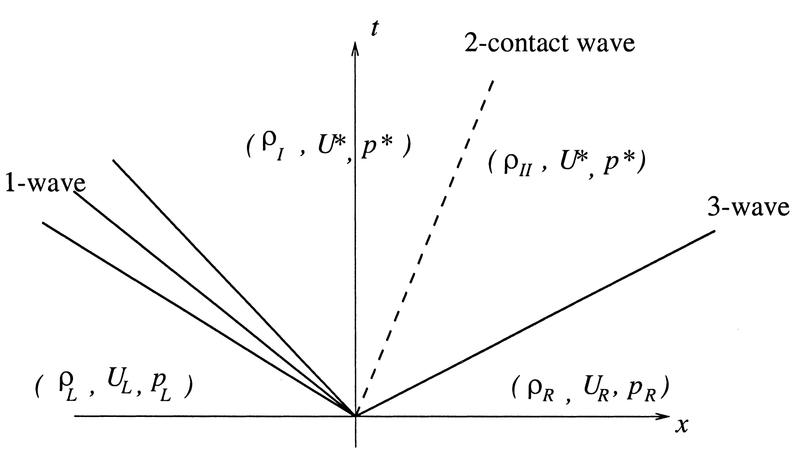

Figure 9. Solution of the Riemann problem in the (x, t)-plane.

Riemann solution could only construct a zero thickness shock structure. If the above shock front is not located exactly at a cell interface, the shock waves generated in the Riemann solutions at adjacent cell boundaries will become even weaker, and they introduce even less physical dissipation. Therefore, the main dissipation in the Godunov method must come from other sources.

Besides the above physical dissipation, the numerical dissipation in the Godunov method is coming from the averaging stage [16]. For example, in Figure 10 at the time step $t = t_{n+1}$, the wave structure inside cell j is lost due to the formation of a constant state. This averaging

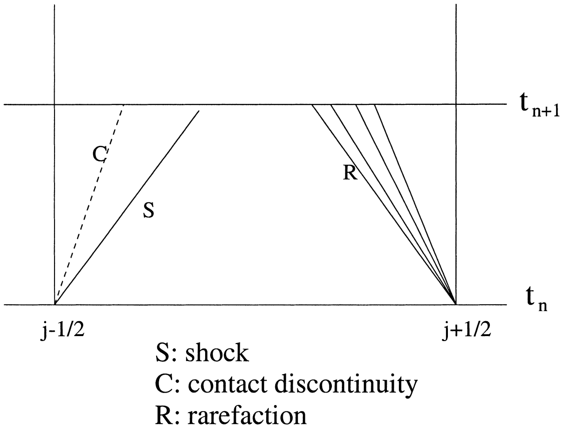

Figure 10. Averaging process at the time step t_{n+1}, where only the total mass, momentum and energy are updated inside cell j. The smearing of the subcell structure is associated with the numerical dissipation.

process is accompanied also by an entropy increase, and introduces numerical dissipation. In the two-dimensional case, for any flow distribution with velocity $(U_1(x, y), U_2(x, y))$ and density $(\rho_1(x, y), \rho_2(x, y))$, the amount of dissipation introduced in each cell due to the averaging is equal to

$$\Delta E_k = E_k - \bar{E}_k \tag{4.4}$$

where E_k is the total kinetic energy before the averaging and $\bar{E}_k$ is the kinetic energy after the averaging. The difference in the kinetic energy is translated into thermal one. As an example, we consider a flow distribution in the two cases in Figure 11, where there are two states $(\rho_1, \mathbf{U_1})$ and $(\rho_2, \mathbf{U_2})$ which occupy equal volumes in both cells. From the conservations of the mass and momentum, we have

$$\bar{\rho} = \frac{1}{2}(\rho_1 + \rho_2)$$

and

$$\bar{\rho}\bar{\mathbf{U}} = \frac{1}{2}(\rho_1\mathbf{U_1} + \rho_2\mathbf{U_2})$$

As a result, the kinetic energy before the averaging is

$$E_k = \frac{1}{4}(\rho_1(\mathbf{U_1})^2 + \rho_2(\mathbf{U_2})^2)$$

and after the averaging

$$\bar{E}_k = \frac{1}{2}\bar{\rho}\bar{\mathbf{U}}^2$$

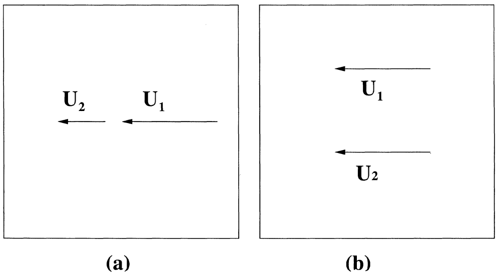

Figure 11. Two initial velocity distributions inside a numerical cell. After averaging, a uniform velocity inside each cell is obtained.

The difference in the kinetic energy is

$$\Delta E_{\mathrm{k}} = \frac{1}{4}\frac{\rho_1\rho_2}{\rho_1+\rho_2}(\mathbf{U_1}-\mathbf{U_2})^2$$

So, the averaging stage in the Godunov method provides the following dissipation

$$\text{dissipation} \sim \frac{\rho_1\rho_2}{\rho_1+\rho_2}(\mathbf{U_1}-\mathbf{U_2})^2 \tag{4.5}$$

In case (a) of Figure 11, a velocity jump from $\mathbf{U_1}$ to $\mathbf{U_2}$ will introduce numerical dissipation automatically. In case (b) of Figure 11, due to the same velocity $\mathbf{U_1} \simeq \mathbf{U_2}$, the numerical dissipation introduced in the averaging stage diminishes. Since the flow distributions $\mathbf{U_1}$ and $\mathbf{U_2}$ inside each cell are closely related to the mesh construction, the dissipation provided in the averaging stage is therefore mesh-oriented. For example, if a two-dimensional normal shock is in the x-direction and the mesh is also constructed along the x- and y-directions, the velocity distribution in the x-direction in the cell around the shock front will be similar to that in Figure 11(a). Along the y-direction, the velocity distribution at the shock front cell is close to that shown in Figure 11(b).

4.2. The explanation of shock instability

The documented observations of shock instability are scattered in many papers. The influential paper by Quirk for the first time systematically presented the observation and analysis [7]. Since then, the explanation of numerical shock instability has attracted much attention in recent years. A short list of references includes [4–6,9] and references therein.

In order to have shock instability, such as the carbuncle phenomena or odd–even decoupling, the numerical shock front has to be aligned with the mesh. As a result, the averaging dissipation (4.5) can be provided mainly in the direction normal to the shock front, such as in the x-direction as shown in Figure 11(a). In the direction along the shock front, such as shown in Figure 11(b), due to the equal velocities and the perfect ability of keeping the shear layer in the exact Riemann solver, neither the numerical dissipation from the averaging, nor the physical dissipation in the Riemann solution, will be provided.

Now let's consider a stationary shock in the x-direction. As shown in Figure 12, the shock front can be divided into supersonic $M>1$ and subsonic $M<1$ regions. There is a sonic line $M=1$ between them. Inside the shock layer, numerical perturbation will most likely disturb the fluid path away from the straight lines. As a result, the fluid trajectory can be considered as moving in the quasi-one-dimensional nozzles. From the aerodynamics, we have

$$\frac{\mathrm{d}U}{U} = -\frac{1}{1-M^2}\frac{\mathrm{d}S}{S}$$

and

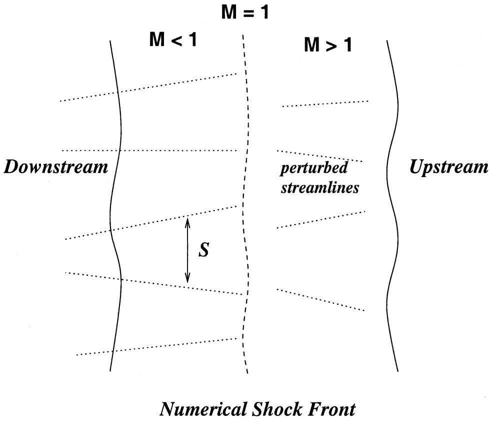

Figure 12. A numerical normal shock in the two-dimensional case. Due to the numerical perturbations, the fluid path will deviate from the straight lines to form the quasi-one-dimensional flows. In the supersonic side $M > 1$, the numerical structure is stable to perturbation. In the subsonic side $M < 1$, the perturbation will be amplified to form instability.

$$\frac{\mathrm{d}p}{p} = \frac{\gamma M^2}{1 - M^2}\frac{\mathrm{d}S}{S}$$

where S is the cross section, M is the mach number, and $\mathrm{d}U$ and $\mathrm{d}P$ are the velocity and pressure changes along the fluid motion.

Case (1): For $0 \le M \le 1$, an increase in velocity is associated with a decrease in area, and vice versa. Therefore, the velocity increases (pressure decreases) in a converging streamline case and velocity decreases (pressure increases) in a diverging streamline case.

Case (2): For $M > 1$, the velocity increases (pressure decreases) in the diverging streamline case and velocity decreases (pressure increases) in the converging streamline case.

In the subsonic region, once there is perturbation inside the numerical shock layer, an increase of velocity is associated with a decrease of pressure, and the converging of streamlines. Physically, the shear viscosity will strongly take effect to reduce the velocity differences and stabilize the numerical shock structure. However, following the inviscid Euler solution (Riemann problem) in the y-direction, the only dynamical influence involved in the exact Riemann solution in this direction is the slight pressure difference. The fluid in the higher pressure region will move toward to the low pressure region. As a consequence, in the subsonic side the fluid pressure in the low pressure region will get even lower, and the high velocity gets even higher in the converging streamline case. So, is the instability formed. The instability also happens in the diverging streamline case in the subsonic region.

In the supersonic region, in the converging streamline case an increase in velocity will be associated with an increase in pressure. So, the central high pressure region could expand and stop the converging of the streamlines. Therefore, in the upstream side with $M > 1$, the flow structure is basically stable to any small perturbation.

Figure 13 shows the density distributions in Figure 6(a) along the x-direction at different y locations, which clearly shows that the density fluctuation gets amplified in the downstream region $M < 1$. The numerical observation confirms the above analysis.

The above analysis of the dissipative mechanism in the Godunov method also validates the following numerical observation. If the shock front is not precisely aligned with the mesh, the velocity differences between U_1 and U_2 will appear in both directions around the shock front. As a result, the averaging dissipation will be provided in both directions. For example, when the shock front in Figure 6 is tilted by 10°, the new density distribution in the shock tube is shown in Figure 14, where the averaging dissipation takes effect in both directions to eliminate the shock instability.

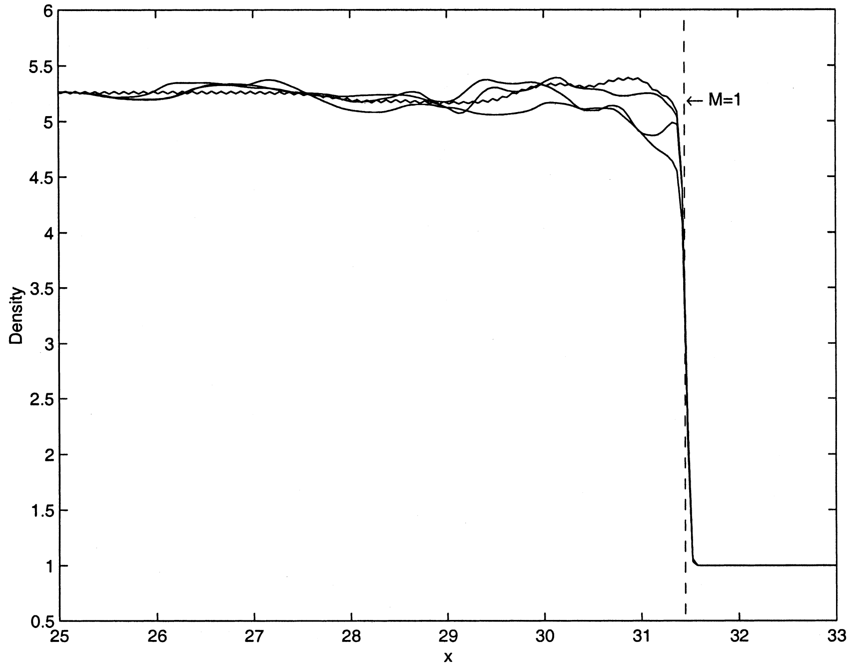

Figure 13. Density distributions of Figure 6(a) along the x-direction at different y locations. The density fluctuation is amplified in the downstream region $M < 1$, which is consistent with the physical argument in the current paper and Figure 12.

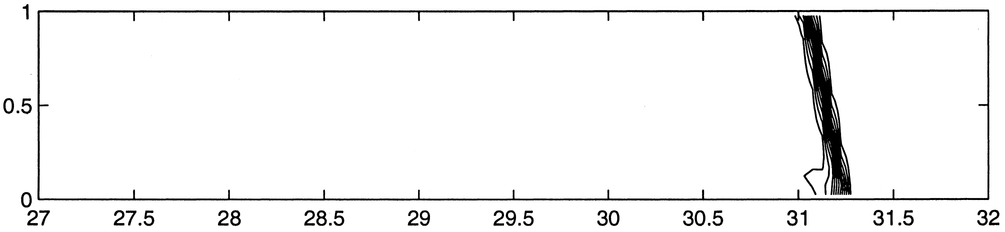

Figure 14. Density distribution calculated by the second-order Godunov method for the inviscid Euler equations. The shock jump and the flow perturbation are the same as that in Figure 6(a) except the normal shock front is tilted by 10° with respect to y-axis. As a result, the numerical dissipation due to averaging takes effect in both directions. Any post-shock oscillation is Figure 6(a) is effectively eliminated.

5. CONCLUSION

In this paper, we have tested the Godunov and the FVS schemes in the shock structure, boundary layer, and two-dimensional shock tube cases. At the same time, we analyze the dissipative mechanism in both schemes. The conclusion is that for the FVS schemes the numerical viscosity coefficient intrinsically rooted in the flux function is proportional to the cell size $\nu_{\text{num}} \sim \Delta x$. This is related to the wave free transport mechanism in the FVS schemes. Therefore, the FVS scheme is basically solving a viscous governing equation and the viscosity coefficient in the numerical fluid depends on the local mesh size. Even with the varying numerical viscosity coefficient, the dissipative mechanism in the FVS scheme are basically consistent with the Navier–Stokes terms. This is one of the reasons for the robustness of the FVS scheme. Also, the reason for the different behaviors of the FVS schemes in the shock and boundary layer calculations is pointed out.

On the other hand, the Godunov method gives accurate results in both shock structure and boundary layer calculations due to its absence or minimal dissipation in the exact Riemann solution. The necessary numerical dissipation in the Godunov method is solely coming from numerics, such as the averaging process in the construction of the constant state inside each cell. Unfortunately, this kind of dissipation depends on both the flow distribution and the mesh construction, and they are not always consistent with the Navier–Stokes viscous terms. The absence of numerical and physical dissipation in special cases could amplify the shock instabilities.

ACKNOWLEDGMENTS

We would like to thank Professor Hui for helpful discussions. Support was provided by the Hong Kong Research Grant Council through RGC97/98.HKUST6166/97P.

APPENDIX A. THE NUMERICAL VISCOUS EFFECT IN THE VAN LEER FVS SCHEME

For two adjacent cells inside the boundary layer in the y-direction, the flow distribution can be described by the following figure.

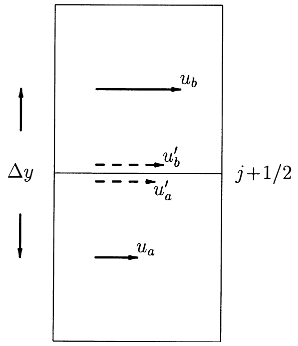

For a second-order scheme, from the cell averaged velocities u_a, u_b, and the corresponding values in surrounding cells, we can use the van Leer limiter to get u'_a and u'_b as the interpolated velocities at the cell interface $j+1/2$. Due to the differences in the magnitudes of u'_a and u'_b, the van Leer splitting flux function gives a net flux of x-momentum transport across the cell interface, which has the amount of

$$\tau = \frac{1}{4}\rho c(u'_b - u'_a) \tag{5.6}$$

where c is the sound speed. At the same time, according to the shear stress definition, we have

$$\tau = \rho\nu \frac{du}{dy} \tag{5.7}$$

and du/dy can be formally defined as

$$\frac{du}{dy} = \frac{u_b - u_a}{\Delta y}$$

From Equations (5.6) and (5.7), we get the following viscosity coefficient ν in the second-order van Leer FVS scheme

$$\nu = \frac{1}{4} c \frac{u'_b - u'_a}{u_b - u_a} \Delta y \tag{5.8}$$

The above linear relation between ν and cell size Δy is consistent with the numerical observation in Section 2. For the first-order FVS scheme, the numerical viscosity coefficient becomes

$$v = \frac{1}{4} c \Delta y$$

Now let's apply Equation (5.8) to the Blasius boundary layer solution. First, taking a few points in the boundary layer, such as

η	0.4	1.2	2.0	2.8
u	0.13277	0.39378	0.62977	0.81152

from which we have $u_{\mathrm{a}} = 0.39378$ and $u_{\mathrm{b}} = 0.62977$. The van Leer limiter then gives $u'_{\mathrm{a}} = 0.5177$ and $u'_{\mathrm{b}} = 0.5271$. In the laminar boundary case in Section 2, we have the pressure $p = 9/(\gamma M^2) = 71.4$ and the sound speed $c = \sqrt{\gamma p/\rho} = 9.997$. Therefore, the numerical viscosity coefficient becomes

$$v = \frac{1}{4} c \frac{u'_{\mathrm{b}} - u'_{\mathrm{a}}}{u_{\mathrm{b}} - u_{\mathrm{a}}} \Delta y = 0.099 \Delta y$$

which has a good agreement with the numerical observation in Section 2, i.e. $v_{\mathrm{num}} = 0.11 \Delta y$. For the first-order FVS scheme, the numerical viscosity coefficient becomes $v = 2.449 \Delta y$, which is much larger than that in the so-called second-order scheme.

As observed in Equation (5.8), the viscosity coefficient depends on the interpolated velocities at the cell interface u'_{a} and u'_{b}. Theoretically, if a third-order interpolation is used, the difference between the values u'_{a} and u'_{b} will be on the order of $O((\Delta y)^2)$, so is the viscosity coefficient. Practically, many high-resolution FVS schemes have been developed for the Navier–Stokes equations [2]. But, the performance of these schemes based on the FVS flux function will depend sensitively on the interpolation method. In the coarse mesh case, such as with five or six grid points in the boundary layer, it is hard to imagine that there would be a perfect interpolation technique to remedy the deficiency in the physical model. Even though high-order interpolation could reduce the numerical dissipation in the FVS scheme, it does not remove the problem from the root. This can be clearly understood when we compare the FVS scheme and the Godunov method. For the Godunov method, whatever the interpolated values u'_{a} and u'_{b} are, it will always keep the velocity difference and give zero x-momentum transport due to its correct capturing of the inviscid Euler solutions. But, the FVS scheme tells a different story once there is any velocity difference between u'_{a} and u'_{b}. Note that the Godunov method will also tell us a different story if the shear layer is not aligned with the mesh distribution, where the averaging dissipation may poison the physical solution.

REFERENCES

1. Chou SY, Baganoff D. Kinetic flux-vector splitting for the Navier–Stokes equations. *Journal of Computational Physics* 1997; **130**: 217–230.
2. Drikakis D, Tsangaris S. On the solution of the compressible Navier–Stokes Equations using Improved Flux Vector Splitting Methods. *Applied Mathematical Modeling* 1993; **17**: 282–297.

3. Godunov SK. A difference scheme for numerical computation of discontinuous solutions of hydrodynamic equations. *Math Sbornik* 1959; **47**: 271.
4. Gressier J, Moschetta JM. On the pathological behavior of upwind schemes. AIAA 98-0110, 1998.
5. Liou MS. Probing numerical fluxes, positivity, and entropy-satisfying property. AIAA 97-2035, 1997.
6. Pandolfi M, D'Ambrosio D. Upwind methods and carbuncle phenomenon. In *Computational Fluid Dynamics '98*, 4th ECCOMAS, Athens, vol. 1, Papailiou KD, Tsahalis D, Periaux J (eds). John Wiley & Sons Ltd: Chichester, 1998; 126–131.
7. Quirk J. A contribution to the great Riemann solver debate. *International Journal for Numerical Methods in Fluids* 1994; **18**(6): 557–574.
8. Roe PL. Approximate Riemann solvers, parameter vectors and difference schemes. *Journal of Computational Physics* 1981; **43**: 357.
9. Sanders R, Morano E, Druguet MC. Multidimensional dissipation for upwind schemes: stability and applications to gas dynamics. *Journal of Computational Physics* 1998; **145**: 511–573.
10. Sod G. A survey of several finite difference methods for systems of nonlinear hyperbolic conservation laws. *Journal of Computational Physics* 1978; **27**: 1–31.
11. Steger J L, Warming R F. Flux vector splitting of the inviscid gas-dynamic equations with applications to finite difference methods. *Journal of Computational Physics* 1981; **40**: 263–293.
12. Toro E. *Riemann Solvers and Numerical Methods for Fluid Dynamics*. Springer: Berlin, 1997.
13. van Leer B. Towards the ultimate conservative difference scheme. IV. A new approach to numerical convection. *Journal of Computational Physics* 1977; **23**: 276–299.
14. van Leer B. Flux-vector splitting for the Euler equations. ICASE Report, No. 82-30, 1982.
15. Xu K. Gas-kinetic schemes for unsteady compressible flow simulations. In *VKI for Fluid Dynamics Lecture Series 1998-093. Computational Fluid Dynamics*, 1998.
16. Xu K, Hu J. Projection dynamics in Godunov-type schemes. *Journal of Computational Physics* 1998; **142**: 412–427.